PCCP

ROYAL SOCIETY OF CHEMISTRY

PAPER

Cite this: *Phys. Chem. Chem. Phys.*, 2023, **25**, 17370

Formation and fragmentation of 2-hydroxyethylhydrazinium nitrate (HEHN) cluster ions: a combined electrospray ionization mass spectrometry, molecular dynamics and reaction potential surface study†

Wenjing Zhou, [ab] Jianbo Liu, *[ab] Steven D. Chambreau [c] and Ghanshyam L. Vaghjiani [d]

Received 5th June 2023,
Accepted 15th June 2023

DOI: 10.1039/d3cp02610h

rsc.li/pccp

The 2-hydroxyethylhydrazinium nitrate ($[HOCH_2CH_2NH_2NH_2]^+NO_3^-$, HEHN) ionic liquid has the potential to power both electric and chemical thrusters and provide a wider range of specific impulse needs. To characterize its capabilities as an electrospray propellant, we report the formation of HEHN cluster ions in positive electrospray ionization (ESI) and their collision-induced dissociation. The experiment was carried out using ESI guided-ion beam mass spectrometry which mimics an electrospray thruster in terms of ion emission, injection into a vacuum and fragmentation in space. Measurements include compositions of primary ions in the electrospray plume and their individual dissociation product ion cross sections and threshold energies. The results were interpreted in light of theoretical modeling. To determine cluster structures that are comprised of $[HE + H]^+$ and NO_3^- constituents, classical mechanics simulations were used to create initial guesses; and for clusters that are formed by reactions between ionic constituents, quasi-classical direct dynamics trajectory simulations were used to mimic covalent bond formation and structures. All candidate structures were subject to density functional theory optimization, from which global minimum structures were identified and used for construction of reaction potential energy surface. The comparison between experimental values and calculated dissociation thermodynamics was used to verify the structures for the emitted species $[(HEHN)_nHE + H]^+$, $[(HEHN)_n(HE)_2 + H]^+$, $[(HE)_{n+1} + H]^+$ and $[(HE)_nC_2H_4OH]^+$ (n = 0–2), of which $[(HE)_{1-2} + H]^+$ dominates. Due to the protic nature of HEHN, cluster fragmentation can be rationalized by proton transfer-mediated elimination of HNO_3, HE and $HE{\cdot}HNO_3$, and the latter two become dominant in larger clusters. $[(HE)_2 + H]^+$ and $[(HE)_nC_2H_4OH]^+$ contain H-bonded water and consequently are featured by water elimination in fragmentation. These findings help to evaluate ion formation and fragmentation efficiencies and their impacts on electrospray propulsion.

1 Introduction

Ionic liquids (ILs), defined as compounds completely composed of ions with melting points at or less than 100 °C,[1,2] have applications ranging from tailored solvents for synthesis and catalysis,[3,4] electrolytes in fuel cells[5] and batteries,[6] potential materials for CO_2 capture and utilization, to explosives and propellant fuels.[7–10] The list of applications continues to expand. Owing to their reduced toxicity and improved performance, ILs have been considered as green alternatives to the current, but toxic, volatile and sensitive monopropellant hydrazine.[11] Since 2003, ILs have been envisioned and fielded as electrospray propellants due to their inherent ionic nature, negligible vapor pressure, higher electrical conductivities and lower viscosities than conventional salt-solvent systems.[12–17]

[a] *Department of Chemistry and Biochemistry, Queens College of the City University of New York, 65-30 Kissena Blvd., Queens, New York 11367, USA. E-mail: jianbo.liu@qc.cuny.edu; Tel: +1-718-997-3271*
[b] *PhD Program in Chemistry, the Graduate Center of the City University of New York, 365 5th Ave., New York, New York 10016, USA*
[c] *Jacobs Technology, Inc., Air Force Research Laboratory, Edwards Air Force Base, California 93524, USA*
[d] *In-Space Propulsion Branch, Rocket Propulsion Division, Aerospace Systems Directorate, Air Force Research Laboratory, AFRL/RQRS, Edwards Air Force Base, California 93524, USA*

† Electronic supplementary information (ESI) available. See DOI: https://doi.org/10.1039/d3cp02610h

Such versatile properties make ILs prime candidates[18] for a dual-mode spacecraft propulsion system,[19] which can operate using a single propellant in either a chemical[20,21] or an electrospray mode[14] as the need arises.

The target IL in the present work is 2-hydroxyethylhydrazinium nitrate ($[HOCH_2CH_2NH_2NH_2]^+NO_3^-$, abbreviated as HEHN). HEHN is a protic IL,[1,22] which can be produced by the stoichiometric neutralization of 2-hydroxyethylhydrazine (HE) with HNO_3. It was developed by the Air Force Research Laboratory (AFRL) as a catalytic monopropellant for chemical propulsion.[23] HEHN is a liquid at room temperature with a glass transition temperature (T_g) of 216.1 K[23] and a melting point of 228 K.[24] Research on the thermal decomposition mechanisms of HEHN has been insightful but limited.[23,25–27] Chowdhury and Thynell[25] investigated the reactions governing the initial decomposition of HEHN using confined rapid thermolysis coupled with FT-IR and time-of-flight mass spectrometry. The results led to a hypothetical kinetics model consisting of a proton transfer reaction in the ion pair to form HE and HNO_3, followed by an autocatalytic reaction between HEHN and HNO_3, ultimately leading to the production of H_2O, N_2O, N_2, O_2 and CH_3CHO. The decomposition kinetics of HEHN was later refined by Esparza *et al.*[26] to accommodate a two-stage activation mechanism, in which the first stage generates H_2O, N_2, NH_3, NO, N_2O and NO_2 and the second stage generates additional gas products HNO_3 and CO_2. More recently, Chambreau, Vaghjiani and co-workers[27] reported exhaustive measurements on HE and HEHN using vacuum ultraviolet photoionization mass spectrometry of supersonic beam, effusive beam and aerosol,[28–30] nanotip ambient ionization mass spectrometry,[31] and laser desorption ionization droplet delivery mass spectrometry.[32] Both flash pyrolysis and unimolecular photodissociation of HE and HEHN were examined, and thermal *vs.* heterogeneous catalytic decomposition were compared. The complementary measurements verified the formation of $^\bullet C_3H_3$ (propargyl), $^\bullet CH_3$, NH_3, H_2O, C_2H_4, H_2CNH, NO, N_2O, $HOCH_2CH_2NH_2$, HNO_3 and HE as well as products of high mass-to-charge ratios (m/z).

Investigations into the electrospray thruster applications of HEHN have emerged recently. Prince *et al.*[14] reported the electrospray mass spectra of HEHN in a positive mode in 2012. Later, Patrick *et al.*[33] reported collision-induced dissociation (CID) of the protonated $[(HE)_2 + H]^+$ and $[(HEHN)_2HE + H]^+$ cluster ions formed in the positive electrospray. Recently, Zeng *et al.*[34] explored the structural features and H-bonding motifs in $[(HEHN)_nHE + H]^+$ (n = 1–5) using cryogenic vibrational spectroscopy. On the basis of classical molecular dynamics simulations, Prince *et al.*[17] determined the Eyring–Polanyi and Arrhenius parameters, rate constants and branching ratios for the unimolecular dissociation of $[(HEHN)_nHE + H]^+$ (n = 1–3).

The principle and techniques of the electrospray thruster have been discussed in many works.[14,16,17,33,35–47] In brief, a high electric field is applied to ILs at a spray emitter leading to the formation of a Taylor cone at the emitter tip[12,48] and the emission of charged IL droplets and ions from the Taylor cone into the gas phase. As the emitted charged species are accelerated in a high electric field to produce a thrust, the spacecraft is accelerated in the opposite direction to the ions. Theoretically, no decomposition of the emitted ions is needed (this is different than chemical propulsion wherein energetic ILs undergo hypergolic ignition upon contact with propulsion oxidizers and produce gaseous products[19,20]). Note that a spacecraft orbiting the Earth may experience extreme temperatures depending on its location with respect to the sun or a shadow (cast by a planet) and altitude. The lowest temperature in the low-Earth orbital (LEO) is 208 K, that in the geosynchronous Earth orbital (GEO) is 77 K, and that in a trans-atmospheric vehicle may go down to 73 K.[49] To this end, the wide liquid range of ILs makes ILs advantageous to move through liquid handing systems without requiring too much on-board power reserves in the spacecraft for thermal control. In addition, a fraction of the electric power fed into the IL electrospray is automatically dissipated as heat and causes a temperature increase in cone-jets of ILs. This process, referred to as self-heating, is generated by cone-jet ohmic and viscous dissipation occurring at sufficiently high conductivities and low Reynolds numbers.[50] The self-heating can raise the temperature sufficiently to alter the physical properties of liquids.[51]

The electrospray emitter may operate in two theoretical conditions as well as a mixed mode between the two extremes.[14] The first extreme, designated as a droplet mode, is dominated by the emission of large droplets containing 10^2–10^3 molecules per charge and hence presents large m/z. The droplet mode produces a large thrust (F) that is proportional to $\sqrt{m/z}$. The second extreme is a purely ionic mode where the emission is dominated by small ions with large ratios of z/m.[17,36,40] In the purely ionic mode, every ion is efficiently used, resulting in a high specific impulse (I_{sp}, the change in momentum per unit mass for rocket fuels, a key metric in assessing propulsion efficiency) that is proportional to $\sqrt{z/m}$.[14]

In the electrospray thruster, greater than 90% propellant utilization is desired for mission planning,[35] yet many factors result in deviations from the theoretical optimum. One such factor arises from the nature of protic ILs[1,22] and their ionicity. Protic ILs have a proton on the cation that can undergo reversible proton transfer with the anion. Depending on several factors including anion basicity, there exists an association equilibrium to form neutral molecules or clusters in the electrospray plume.[1] Consequently, a small fraction of the propellant mass becomes unavailable for ion-thrust generation.

Formation of cluster ions[52–54] and nanoclusters[55] represents another complication associated with electrospray. As the outcome of kinetics-controlled in-source cluster formation and in- and after-source cluster fragmentation may not be accurately predicted on the sole basis of thermodynamics, molecular dynamics simulations are needed to elucidate mechanisms of these events.[53,54] For the electrospray thrusters operating in the purely ionic regime, formation of undesirable IL cluster ions,[17,33,40,41,43] in addition to single ions, brings about several specific issues: (1) I_{sp} of the propellant is decreased by large cluster ions; (2) cluster ions of the same charge but different

masses are accelerated to different final velocities and momenta by the same electric field, and the resulting ion-beam polydispersity limits the propulsion efficiency;[35,39] (3) cluster ions are metastable (lifetime of μs)[40] and undergo in-flight dissociation.[56] Cluster fragmentation may occur *via* various mechanisms in a spacecraft, *e.g.*, the emitted species strike a downstream surface (*i.e.*, liberation of materials in sputtering),[46,47] the backscattering clusters (happening in a bipolar electrospray thruster) impact the surface of the spacecraft,[16] and collisions between the emitted species in ''traffic jams'' within the electrospray plume (because of the differences in their velocities).[42] Cluster fragmentation within the acceleration zone poses a detriment to the propulsion efficiency, namely kinetic energy loss from neutral fragments that are not subsequently accelerated to the theoretical kinetic energy;[17,37,38] and (4) neutral fragments participate in subsequent ion-neutral collisions, further reducing propellant performance and complicating the plume compositions.

These facts indicate that the performance of an electrospray thruster directly depends on formation and reactions (including fragmentation) of the IL cluster ions formed in the spray plume. Electrospray ionization (ESI) mass spectrometry closely mimics the electrospray thruster in terms of ion emission from a Taylor cone, injection into a vacuum, and inherent gas-phase ion chemistry associated with post-extraction activation and fragmentation.[44,57] For this reason, in the present work, ESI mass spectrometry was utilized to examine the compositions, structures, stabilities and primary/secondary reactions of the HEHN cluster cations.

The remainder of the paper is organized as follows. The instrumentation and experimental methods are described in Section 2, including measurements of primary cluster ions and characterization of their kinetic energy dependent CID. The computational methods are described in Section 3. This section starts with two different molecular dynamics simulation approaches for the search of candidate molecular structures for cluster ions. For the cluster ions that are comprised of ionic constituents only, classical molecular mechanics was used for the search of candidate structures; and for the cluster ions that involve chemical reactions and formation of covalent bonds between constituents, quasi-classical direct dynamics was applied. The section then proceeds to the quantum chemistry calculations of the candidate structures acquired from dynamics simulations, followed by calculations of reaction potential energy surfaces (PESs) and thermodynamics using global minimum cluster structures. In Section 4, we report the mass spectrum of HEHN cluster ions in the positive ESI, and the tandem mass spectra of CID product ions for individually selected cluster ions. For each product channel, dissociation energy was determined by analyzing the kinetic energy-dependent cross section for the product ion, and the result was compared to the calculated thermochemistry for a proposed structure. In Section 5, we summarize formation, structures, and fragmentation pathways and energetics for all of the HEHN cluster ions, and their interconversions. Finally, conclusions are presented in Section 6.

2 Experimental methods

2.1 ESI guided-ion beam tandem mass spectrometry and experiment

Formation of the HEHN cluster ions was made through the electrospray of a HEHN solution, followed by two types of measurements: measurement of cluster ion compositions in the electrospray plume, and characterization of cluster ion structures. Both measurements were carried out on a home-built guided-ion beam tandem mass spectrometer located at Queens College.[58] In structural characterization, cluster ions of specific m/z were selected and underwent CID with the inert Xe atoms through the use of ion-neutral scattering techniques[59–61] incorporated into the tandem mass spectrometer. The apparatus along with operation and calibration was reported in detail before.[58] A brief description is given here, emphasizing the instrumentation parameters used in the work.

The HEHN sample (received from AFRL, Edwards AFB, containing 4.5% water) was diluted to 5 mM in a solvent of 75% CH_3CN and 25% water. The solution was sprayed into the ambient atmosphere (flow rate 0.06 mL h^{-1}) through a 35-gauge stainless steel electrospray needle (OD 0.005 inch, ID 0.0021 inch, biased at 3.2 kV relative to ground). ESI-formed charged droplets entered the mass spectrometer through a pressure-reducing capillary heated to 455 K and biased at 70–180 V relative to ground. Liquid aerosols underwent desolvation within the capillary, and were ultimately converted to gaseous cluster ions. A skimmer of 1.0 mm-diameter orifice is located at 3 mm away from the end of the capillary. The skimmer was biased at 15–30 V relative to ground. The electric field between the end of the capillary and the skimmer served three purposes: to remove remaining solvent molecules attached to ions *via* collision-induced desolvation by the background gas of 1.7 torr in the source chamber;[62] to prevent large solvent clusters from appearing downstream;[63,64] and to promote in-source dissociation of larger clusters. Ions that passed through the skimmer were transported into a radio-frequency (rf) hexapole ion guide. The interaction of ions with the background gas (at a pressure of 20 mTorr) within the rf hexapole led to ion energy dissipation and focusing,[65–67] through which the ion internal energy was thermalized to 310 K[58] and the kinetic energy spread was narrowed down to within 0.6 eV FWHM (full-width at half-maximum).

For measurement of the HEHN ion plume compositions, the first quadrupole mass filter in the tandem mass spectrometer was operated in a rf-only mode (*i.e.*, removing the resolving DC potential) to transmit all ions. A mass scan was performed by a second quadrupole mass filter, and ions were counted by an off-axis electron multiplier. For measurement of tandem CID product ions, cluster ions were mass selected in the first quadrupole mass filter before injection into an octopole ion guide. Along the octopole ion guide, ions passed through a 10 cm-length scattering cell containing the Xe gas. In addition to providing a rf potential that traps ions in the radial direction, the octopole ion guide was biased at a DC offset potential. The DC potential allowed the control of the kinetic energy of

primary ions in the laboratory frame (E_{lab}), thereby setting the collision energy (E_{CM}) between ions and the Xe gas in the center-of-mass frame, that is $E_{CM} = E_{lab} \times m_{neutral}/(m_{ion} + m_{neutral})$, where $m_{neutral}$ and m_{ion} are the masses of Xe and primary ions, respectively. CID was measured over a broad range of E_{CM}, from which kinetic energy-dependent dissociation was detected. The Xe gas pressure was maintained at no more than 0.03 mTorr through a leak valve and measured using a capacitance manometer. At this target gas pressure, most of the primary ions underwent at most single collisions with the Xe gas. The probability of ions having single collisions with Xe was 5%, that of double collisions with Xe was $<0.2\%$, and that of having more than double collisions was negligible. After CID, product ions and remaining reactant ions were collected by the octopole, passed into the second quadrupole for mass analysis and counting.

2.2 Data analysis

Dissociation product ion cross section. As ion-neutral collisions were carried out at a low target gas pressure to ensure single collision conditions, a thin-target limit based on the Beer–Lambert law[64] could be applied to the calculation of dissociation product ion cross section. Accordingly, the cross section was calculated directly from the ratio of product ion (after correction for the background signal produced from CID occurring outside the scattering cell) to reactant ion intensity, the scattering cell gas pressure and the effective length of the cell. Cross section is a micro-analogue of unimolecular dissociation rate constant k, and cross section = k/v where v is relative velocity.[68] Each product ion channel was measured as a function of E_{CM} over the range of 0.05 to 9 eV. The entire experiment was repeated four times under the same conditions to reduce the standard deviations error in the data.

Dissociation energy at 0 K. Due to the kinetic energy spread and internal energy of the primary ions and the Doppler broadening (*i.e.*, thermal velocity inside the scattering cell) of the Xe gas, CID product ion cross section rises from zero at E_{CM} lower than the true dissociation threshold or activation energy. To determine the exact value of dissociation threshold, the E_{CM} – dependent cross section was analyzed using a modified line-of-centers (LOC) function:[60,68–70]

$$\sigma(E) = \sigma_0 \frac{(E_{CM} + E_{vib} + E_{rot} - E_0)^n}{E_{CM}} \quad (1)$$

where σ_0 is an energy-independent scaling factor, E_{vib} and E_{rot} are reactant vibrational and rotational energies, E_0 is the threshold energy at 0 K, and n is a fitting parameter which determines the efficiency of translational-to-internal energy transfer ($T \rightarrow E_{int}$) in collisions and therefore controls the slope of $\sigma(E)$. The LOC model assumes that a fraction of near-threshold collisions are completely inelastic so that all of the energy contributes to overcome E_0.[60,70,71]

Before comparison with the experimental data, the $\sigma(E)$ function was convoluted over the experimental energy broadening and kinetic factors. To this end, a Monte Carlo classical mechanics simulation program written for ion–molecule collisions[72,73] was used to mimic energy broadening in ion-Xe collisions. For each product channel, a total of 100 000 ion-Xe collisions were simulated at each nominal E_{CM}. In these collisions, the Xe atoms were sampling a Maxwell–Boltzmann kinetic energy distribution at the scattering cell temperature of 300 K. The primary ions were sampling E_{lab} corresponding to the specific E_{CM} with a FWHM of 0.6 eV in the laboratory frame and E_{vib} and E_{rot} from the normalized vibrational and rotational Maxwell–Boltzmann energy distributions at 310 K.

To account for kinetic shift[74] (*i.e.*, excess energy is required to observe detectable dissociation within the ion time-of-flight in the mass spectrometer),[75] each collision that had total energy exceeding E_0 was subjected to Rice–Ramsperger–Kassel–Marcus (RRKM) analysis[76] to determine if it would lead to a dissociation within the ion time-of-flight ($\sim$500 μs) or not. The collision outcomes at various E_{CM} were fed into eqn (1). A leveling-off function was used in the fitting to allow $\sigma(E)$ to reach a plateau at high E_{CM}. The rising curvature of $\sigma(E)$ is highly sensitive to E_0 and n, the values of which were adjusted until the convoluted $\sigma(E)$ matched the experiment. Uncertainties of E_0 were determined from several independent fits using an acceptable range of n and included the absolute uncertainties in E_{CM}.

3. Theoretical methods

3.1 Classical molecular dynamics simulations

Classical molecular dynamics simulations were carried out using the GROMACS software.[77–83] Universal force field and topology files required for the GROMACS simulations were generated by the Sobtop program,[84] for which the Hessian matrices for individual constituents ($[HE + H]^+$, NO_3^-, $[HE + H]^+ \cdot NO_3^-$, and HE) were acquired from the electronic structure calculations using Gaussian 16.[85]

Note that, despite the existence of an isolated stable neutral pair of $HE \cdot HNO_3$ in the gas phase, this neutral pair does not exist within large HEHN cluster ion.[33,34] A relaxed PES scan along the center-of-mass distance between $HE \cdot HNO_3$ and a second $[HE + H]^+$ (Fig. S1 in the ESI,† calculated at the ωB97XD/6-31+G(d,p) level of theory using Gaussian 16) has shown that the neutral $HE \cdot HNO_3$ starts converting to an ion pair even with the presence of a $[HE + H]^+$ at a distance of $\sim$30 Å. This behavior is reminiscent of hydroxylammonium nitrate (HAN).[57] A HAN monomer adopts a stable H-bonded, neutral $HONH_2 \cdot HNO_3$ structure in the gas phase; wherein, spontaneous proton transfer between the $HONH_2$ and HNO_3 moieties is trigged by a charge and/or a dipole of a water molecule without the need for chemical interaction or close physical contact.

For this reason, most HEHN clusters have constituents in their ionic forms, unless otherwise stated. In the GROMACS simulations of this type of cluster ions, their constituents were all inserted into a 3 nm × 3 nm × 3 nm cube. An initial energy-minimization procedure was used to find a potential energy minimum under the *NVT* (constant-temperature and

constant-volume or canonical) ensemble. The resulting minimum-energy structure was used as the starting point in simulated annealing.[86] In brief, the starting structure was subject to temperature ramping from 300 K to 500 K within 3 ps, followed by 4 ps of dynamics at 500 K, and then cooled to 300 K within 3 ps. The acquired candidate structure was then used as a new starting structure and subject to another annealing process.

Following this sequence, 100 candidate structures were generated to cover reasonable cluster conformations, and they were viewed using the VMD program[87] to remove duplicates. All unique structures were submitted to quantum mechanics geometry optimization at the ωB97XD/3-21G level of theory using Gaussian 16. All conformers that were within a 0.5 eV energy range were subject to further optimization using the larger 6-31+G(d) basis set and then the 6-31+G(d,p) basis set, from which their explicit local and global minima were found.

3.2 Quasi-classical, direct dynamics trajectory simulations

To help identify covalent cluster structures that formed *via* ion-molecule reactions, quasi-classical, direct dynamics trajectories were calculated to mimic the formation of cluster ions starting from their constituents and/or fragments. Quasi-classical, direct dynamics avoids the need for an analytical potential; instead, forces needed for trajectory integration are determined ''on the fly'' by calculating the gradient of electronic potential energy at each point in the trajectory.[88–91] Quasi-classical, direct dynamics trajectories were calculated by using a combination of the Venus code of Hase *et al.*[92,93] to set up initial conditions for a series of trajectories and the Gaussian program to integrate the trajectories. Vibrational excitations in the trajectory reactants were sampled using the quantum Boltzmann probability distributions[94] $P(n_i) = \exp(-n_i h\upsilon_i/k_B T)[1 - \exp(-h\upsilon_i/k_B T)]$ where ν_i and n_i are the vibrational frequency and quantum number of the ith mode, respectively, and T is the temperature (310 K) of the reactants. The reactants had zero-point energy (ZPE) in all vibrational modes, and individual reactant atoms were provided momenta and displacements from equilibrium with random phases for different modes. Hessians needed for normal mode calculations were computed at the ωB97XD/6-31G+(d) level of theory. Reactant rotational energy (E_{rot}) was sampled from a classical Boltzmann distribution at 310 K.

Trajectories were started at the randomly oriented reactants with an initial center-of-mass separation of 8.0 Å and E_{CM} of 0.5 eV between the collision partners, and terminated after the formation of a cluster ion or when product separation exceeded 10.0 Å. The E_{CM} chosen for the trajectories was low enough to allow for complex formation in the collisions, but it was not so low as to substantially increase trajectory integration time. For each reaction system, trajectories were collected at three impact parameters (b) to explore different collision dynamics, *i.e.*, b = 0 Å (to mimic head-on collisions), 1.5 Å (a midrange impact parameter to mimic complex formation within the hard-sphere collision radius) and 3.0 Å (a large impact parameter to mimic direct reaction in side-scattering). Using three fixed b values instead of sampling b randomly within a fixed range also allowed us to examine the reaction opacity function, *i.e.*, the b-dependence of reactivity. For each collision system, a total of 300 trajectories were simulated, with 100 each at b = 0, 1.5 and 3.0 Å.

Trajectories were propagated using the Hessian-based method of Bakken *et al.*,[91] implemented in the Gaussian software with Hessians reevaluated every five steps. The propagation step size was set at 0.25 amu$^{1/2}$·bohr (equivalent to a step size of 0.4 fs in trajectory time), to ensure the conservation of energy and momentum. At each point, energies, forces and Hessian were calculated using DFT at the ωB97XD/6-31G+(d) level of theory. This level of theory was chosen based on a compromise between accuracy and computational cost, as previously demonstrated in our simulations of other IL dynamics.[57,95–97]

3.3 PES calculations

After identifying the most probable structure for each cluster ion on the basis of molecular dynamics simulations and quantum chemistry optimization, the last step was to map out cluster reaction coordinates and PES including structures and energies of reactants, transition states (TSs), intermediates and products. PES was calculated using the ωB97XD/6-31+G(d,p) level of theory (unless otherwise stated). TSs were verified as first-order saddle points by frequency calculations, and the vibrational mode with an imaginary frequency corresponds to the reaction coordinate. The intrinsic reaction coordinate was evaluated to further verify that each TS was connected to the correct reactant/product minima. Electronic structure calculations were carried out using Gaussian 16. Cartesian coordinates for all of the calculated species are provided in the ESI.† Cluster ion dissociation energies were calculated at 0 K to allow for a direct comparison with the LOC fits of the CID experiment. Reaction PESs in the ESI† were calculated at 298 K. All energies reported have taken into account ZPEs and thermal corrections (298 K), and ZPEs were scaled by a factor of 0.975.[98]

4 Results and discussion

4.1 Formation of HEHN cluster ions in positive electrospray

Fig. 1 presents a mass spectrum of the HEHN cluster ions produced in the positive electrospray. The species can be grouped into four series $[(HEHN)_nHE + H]^+$, $[(HEHN)_n(HE)_2 + H]^+$, $[(HE)_{n+1} + H]^+$ and $[(HE)_nC_2H_4OH]^+$ (n = 0–2). The first two series are built on the progression of HEHN and the next two are on the progression of HE. The observation of the HE progression agrees with the formation of neutral HE by proton transfer in the protic HEHN IL, and that of $C_2H_4OH^+$ indicates the in-source dissociation of HEHN at the C–N bond. Our measurement has not only reproduced the electrospray mass spectrum of HEHN reported by Prince, Fritz and Chiu,[14] but also discovered the new series $[(HE)_{2-3} + H]^+$ and $[(HE)_{1-2}C_2H_4OH]^+$.

Besides the four major series, ions of m/z 59 may be assigned to a water-elimination product of $[HE + H]^+$, ions of m/z 118 are attributed to the solvated $[HE + H]^+ \cdot CH_3CN$, which disappeared

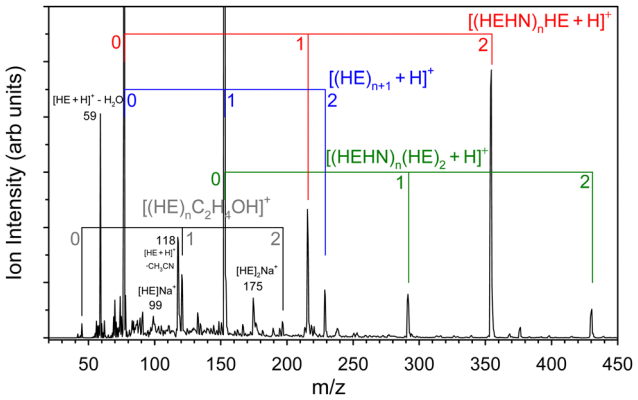

Fig. 1 Formation of HEHN cluster ions in the positive ESI of 5 mM HEHN in 3 : 1 acetonitrile/water. The four major series of ionic species are distinguished by the colors of their labels.

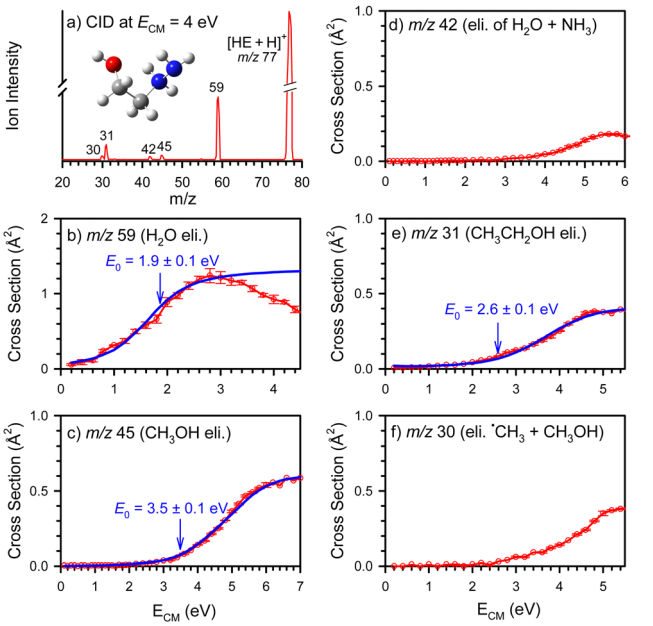

Fig. 2 (a) Structure and a representative CID product ion mass spectrum of $[HE + H]^+$; and (b–f) individual product ion cross sections as a function of E_{CM}, wherein red lines with error bars represent the experimental data and blue lines represent the LOC fits.

completely in the electrospray of HEHN in pure water. Ions of *m*/*z* 175 were also observed in Prince *et al.*'s study but yet unassigned. We tentatively assign *m*/*z* 175 as $[HE]_2Na^+$ on the basis of its CID product ions at *m*/*z* 99 ($[HE]Na^+$) and 23 (Na^+). This assignment is further supported by the elimination of *m*/*z* 23 (Na^+) from the daughter ion $[HE]Na^+$. However, the source of Na^+ remains unclear.

Note that our mass spectrum was acquired by electrospray of a 5×10^{-3} M HEHN solution through a stainless steel emitter. The use of a diluted HEHN solution was necessary for conventional ESI mass spectrometry, as the intensity of ions exhibits a linear dynamic range from the lower limit of detection to 10^{-4}–10^{-5} M (where the intensity increases linearly with increasing concentration), then levels off as a function of increasing concentration, and finally decreases as the concentration is further raised.[99] The mass spectrum of Prince *et al.* was, on the other hand, acquired by field evaporation of pure HEHN IL as in the electrospray thruster.[14] The electrospray thruster uses either a capillary emitter as in our case or an externally wetted needle,[44,100] and both follow the same principle to produce thrust. In Prince *et al.*'s work, HEHN from a reservoir was applied to an externally wetted titanium electrospray emitter. The flow was driven by capillary action as well as surface characteristics of the emitter, and aided by the electric field applied between the emitter and an extractor placed near the emitter tip. When the extraction voltage reached a critical value, field emission occurred. The emitted species have 10^2–10^3 eV kinetic energy. As a result, their quadrupole mass spectrometer had to be modified to tolerate ion kinetic energy at the cost of ion transmission and *m*/*z* resolution. Nevertheless, the overwhelming similarities between the two mass spectra of Prince *et al.* and ours indicate that our ESI mass spectrum was able to capture all important plume compositions in pure HEHN IL electrospray.

4.2 Dissociation of $[(HE)_{n+1} + H]^+$ (n = 0, 1 and 2)

$[HE + H]^+$ (*m*/*z* 77). Despite being the lightest ion selected for CID, $[HE + H]^+$ displays rich fragmentation chemistry. Fig. 2a presents its CID product ion mass spectrum recorded at E_{CM} = 4.0 eV, including *m*/*z* 59 (H_2O elimination), 45 (CH_3OH elimination), 42 (elimination of $H_2O + NH_3$), 31 (CH_3CH_2OH elimination) and 30 (elimination of $CH_3OH + {}^{\bullet}CH_3$). The cross sections for individual product ions were measured over a wide range of E_{CM} and are reported in Fig. 2b–f, wherein error bars were determined on the basis of four sets of measurements.

The blue lines in Fig. 2b, c and e respectively represent the LOC fits for the kinetic energy dependent cross sections of H_2O, CH_3OH and CH_3CH_2OH elimination channels with the values of the fitted dissociation threshold at 0 K, E_0, marked. Note that multiple product channels and branching ratios may be simulated by incorporating a statistical model, such as when using the Crunch program developed by Armentrout, Ervin, Rodgers and co-workers.[74,101,102] However, simultaneous fitting of multiple channels requires the knowledge of dissociation TS properties for each of all product channels. Such fitting became impractical in the present work. For example, the two product channels of *m*/*z* 42 and 30 have high apparent dissociation thresholds, and each involves stepwise elimination of ($H_2O + NH_3$) or ($CH_3OH + {}^{\bullet}CH_3$) through secondary reactions with unknown TSs (interestingly, the elimination of NH_3 or ${}^{\bullet}CH_3$ could not happen in a primary reaction). In our work, LOC fits were carried out without first exploring reaction TSs and PES. The fact that our fits were able to reproduce the E_{CM}-dependent cross sections helped us identify reactant structures and map out reaction PES. Because *m*/*z* 42 and 30 were not produced from primary reactions, we did not attempt to fit their cross sections.

Two structures were proposed for $[HE + H]^+$ with the difference being which amino group is protonated: $[HOCH_2CH_2NH_2NH_2]^+$ *vs.* $[HOCH_2CH_2NHNH_3]^+$. $[HOCH_2CH_2NHNH_3]^+$

has identical energy as that of $[HOCH_2CH_2NH_2NH_2]^+$ at the ωB97XD/6-311++G(d,p) level of theory, but slightly higher (by 0.03 eV) than the latter at the M06-2X/6-311++G(d,p) level. Yet, the interconversion barrier between the two isomers is up to 2.01 eV leading from $[HOCH_2CH_2NH_2NH_2]^+$. We calculated dissociation enthalpies (ΔH, 0 K) resulting from each structure, as well as activation barriers ($\Delta H^{\neq}$, 0 K) for single-step processes, as listed below.

$[HOCH_2CH_2NH_2NH_2]^+$

$\rightarrow [CH_3CH{=}NHNH_2]^+ + H_2O \quad \Delta H = 0.10$ eV ($\Delta H^{\neq} = 1.93$ eV) (2b.1)

$\rightarrow [CH_2{=}NHNH_2]^+ + CH_3OH \quad \Delta H = 1.30$ eV ($\Delta H^{\neq} = 3.39$ eV) (2c.1)

$\rightarrow [CH_2{=}C{=}NH_2]^+ + H_2O + NH_3 \quad \Delta H = 1.06$ eV (2d.1)

$\rightarrow [NH{=}NH_2]^+ + CH_3CH_2OH \quad \Delta H = 2.30$ eV ($\Delta H^{\neq} = 2.53$ eV) (2e.1)

$\rightarrow [N{=}NH_2]^+ + CH_3OH + {}^{\bullet}CH_3 \quad \Delta H = 5.90$ eV (2f.1)

$[HOCH_2CH_2NHNH_3]^+$

$\rightarrow [CH_3CH{=}NNH_3]^+ + H_2O \quad \Delta H = 0.43$ eV ($\Delta H^{\neq} = 2.90$ eV) (2b.2)

$\rightarrow [CH_2{=}NHNH_2]^+ + CH_3OH \quad \Delta H = 1.30$ eV ($\Delta H^{\neq} = 2.82$ eV) (2c.2)

$\rightarrow [CH_2{=}C{=}NH_2]^+ + H_2O + NH_3 \quad \Delta H = 1.06$ eV (2d.2)

$\rightarrow [N{=}NH_2]^+ + CH_3OH + {}^{\bullet}CH_3 \quad \Delta H = 5.90$ eV (2f.2)

It can be seen from above that the activation energies for water, methanol and ethanol elimination from $[HOCH_2CH_2NH_2NH_2]^+$ respectively in reactions (2b.1), (2c.1) and (2e.1) nicely match the corresponding experimental E_0 values. $[HOCH_2CH_2NHNH_3]^+$, on the other hand, cannot eliminate ethanol. Moreover, its activation energies for water and methanol elimination respectively in reactions (2b.2) and (2c.2) significantly deviate from the experimental data. These facts indicate that $[HOCH_2CH_2NH_2NH_2]^+$ represents the dominating $[HE + H]^+$ structure in our experiment.

Concerning the $[HE + H]^+$ structure in the context of IL, the ion-pairing energy is 5.03 eV for $[HOCH_2CH_2NH_2NH_2]^+NO_3^-$ *vs.* 4.87 eV for $[HOCH_2CH_2NHNH_3]^+NO_3^-$ calculated at ωB97XD/6-31+G(d,p). This reaffirms that $[HE + H]^+$ favors the $[HOCH_2CH_2NH_2NH_2]^+$ structure in the HEHN IL. Similarly, for $[HE + H]^+$-containing cluster ions, the structures containing $[HOCH_2CH_2NH_2NH_2]^+$ are 0.09–0.23 eV more stable than those containing $[HOCH_2CH_2NHNH_3]^+$. Therefore, the $[HOCH_2CH_2NH_2NH_2]^+$ structure is adopted here for the cluster ions.

$[(HE)_2 + H]^+$ (m/z 153). The CID of $[(HE)_2 + H]^+$ has demonstrated that the clusters of the same m/z may also adopt quite different structures depending on post-extraction conditions. In this experiment, the post-extraction conditions involve the reactions occurring in the ion source chamber, *i.e.*, within the desolvation capillary and/or between the exit of the desolvation capillary and the skimmer. Two extreme conditions were realized for in-source reactions by adjusting the electric potential between the desolvation capillary and skimmer, each of which is described below:

(1) Condition I, the ion source was adjusted (by floating the desolvation capillary at 183 V and the skimmer at 59 V, *i.e.*, hard in-source collision) to only populate a primary ion structure that did not eliminate water in the subsequent Xe-induced CID. As a result, the CID mass spectrum in Fig. 3a presents only a single product ion $[HE + H]^+$ at m/z 77. Fig. 3b presents the E_{CM}-dependent cross section of the product $[HE + H]^+$. A similar CID result and the corresponding $[HOCH_2CH_2NHNH_2]\cdot[HOCH_2CH_2NH_2NH_2]^+$ structure (referred to as Structure I for $[(HE)_2 + H]^+$, as illustrated in Fig. 3a) were also reported by Patrick *et al.*[33] The calculated ΔH (1.38 eV) for the HE elimination in reaction (3b) is consistent with the experimental E_0 value (1.2 ± 0.2 eV).

$[HOCH_2CH_2NHNH_2]\cdot[HOCH_2CH_2NH_2NH_2]^+$ (Structure I)

$\rightarrow HOCH_2CH_2NHNH_2 + [HOCH_2CH_2NH_2NH_2]^+ \quad \Delta H = 1.36$ eV (3b)

(2) Condition II, the ion source was modified (the desolvation capillary and the skimmer were floated at 80 V and 46 V, respectively, *i.e.*, soft in-source condition) to populate a primary ion structure that presented significant water elimination in

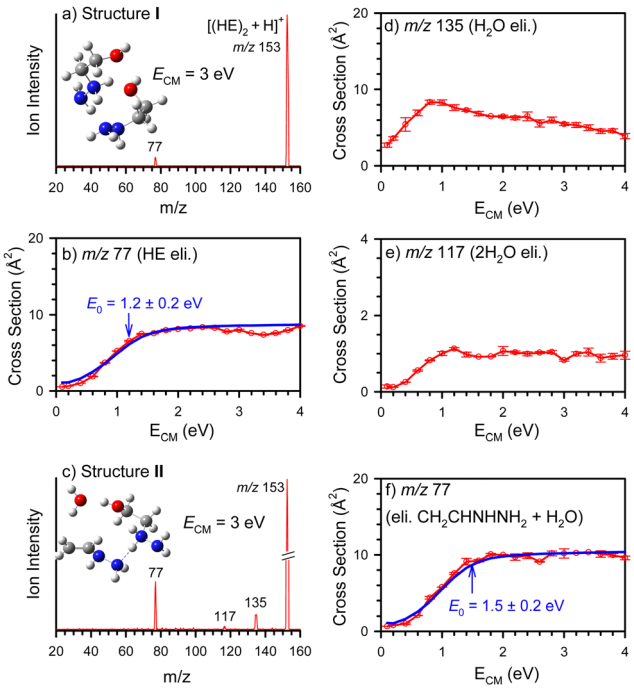

Fig. 3 Structures, CID product ion mass spectra and individual product ion cross sections of (a and b) $[HOCH_2CH_2NHNH_2]\cdot[HOCH_2CH_2NH_2NH_2]^+$ and (c–f) $[CH_2CHNHNH_2]\cdot[NH_2NH_2CH_2CH_2OH]^+\cdot H_2O$. For cross sections, red lines with error bars represent the experimental data and blue lines represent the LOC fits.

the Xe CID. As shown in Fig. 3c, the dissociation of the so-selected m/z 153 structure produced two new product channels in addition to the HE elimination: product ions at m/z 135 corresponding to single-water elimination, and those at m/z 117 representing double-water elimination. Fig. 3d–f present individual product ion cross sections. The cross section for single-water elimination (Fig. 3d) has already risen to 3 Å^2 at the lowest experimental E_{CM}, reaching a maxima at $\sim$1 eV and afterwards decreasing with increasing E_{CM}. This fast-rising cross section is distinctly different than any endothermic product channel with $E_0 \geq 1.2$ eV observed in this study, as the cross section of the latter would present an onset at the low E_{CM} range. It suggests that the threshold energy for single-water elimination must be lower than 1.2 eV. The implication is that the reaction detected in Fig. 3d is not a simple water elimination from a HE or $[HE + H]^+$ moiety, as the water-elimination barriers for HE and $[HE + H]^+$ are 2.95 eV and 1.96 eV, respectively. The question arises as to what structure of m/z 153 (referred to Structure II) was formed under condition II? The low water-elimination energy of Structure II leans toward an H-bonded water complex structure, and we have proposed three reaction scenarios as described below.

The first scenario is initiated by water elimination from $[HE + H]^+$. However, if the structure appears as $[HE]\cdot[HE + H^+ - H_2O]\cdot H_2O$, the fragment ion $[HE + H^+ - H_2O]$ should have been observed at m/z 59; but this was not the case. It follows that the remaining $[HE + H^+ - H_2O]$ (*i.e.*, $[CH_2CH_2NHNH_2]^+$) must have covalently bonded to HE, forming a $[HOCH_2CH_2NHNH_2$-$CH_2CH_2NHNH_2]^+\cdot H_2O$ complex. The PES for the in-source formation and subsequent CID of $[HOCH_2CH_2NHNH_2CH_2$-$CH_2NHNH_2]^+\cdot H_2O$ are provided in Fig. S2 in the ESI,† in which the $[HOCH_2CH_2NHNH_2CH_2CH_2NHNH_2]^+\cdot H_2O$ is located at zero point of the PES. This structure may be converted from $[(HE)_2 + H]^+$ with an activation barrier of 2.09 eV and product enthalpy of +0.38 eV. The cross-linking of $[HE + H^+ - H_2O]$ (*i.e.*, $[CH_2CH_2NHNH_2]^+$) with HE may also lead to a $[HOCH_2$-$CH_2NH(NH_2)CH_2CH_2NHNH_2]^+\cdot H_2O$ structure, as shown in Fig. S3 in the ESI.† However, the formation barrier for $[HOCH_2CH_2NH(NH_2)CH_2CH_2NHNH_2]^+\cdot H_2O$ from $[(HE)_2 + H]^+$ is much higher than that of $[HOCH_2CH_2NHNH_2CH_2CH_2$-$NHNH_2]^+\cdot H_2O$, and no $[HE + H]^+$ elimination pathway was found for $[HOCH_2CH_2NH(NH_2)CH_2CH_2NHNH_2]^+\cdot H_2O$; hence this structure is less likely to be present in the experiment. The dissociation reactions of $[HOCH_2CH_2NHNH_2CH_2CH_2$-$NHNH_2]^+\cdot H_2O$ are presented below:

$$[HOCH_2CH_2NHNH_2CH_2CH_2NHNH_2]^+\cdot H_2O \quad \text{(first probable Structure II)}$$

$$\rightarrow [HOCH_2CH_2NHNH_2CH_2CH_2NHNH_2]^+ + H_2O \quad \Delta H = 0.33 \text{ eV} \qquad (3d.1)$$

$$\rightarrow \textit{cyclo}\text{-}[CH_2CH_2NHNH^+(CH_2CH_2NHNH_2)] + 2H_2O \quad \Delta H = 1.25 \text{ eV } (\Delta H^{\neq} = 2.93 \text{ eV}) \qquad (3e.1)$$

$$\rightarrow [HE + H]^+ + CH_2CHNHNHNH_2 + H_2O \quad \Delta H = 1.42 \text{ eV } (\Delta H^{\neq} = 1.93 \text{ eV}) \qquad (3f.1)$$

The second scenario corresponds to water elimination from HE followed by H-bonding of the resulting $CH_2CHNHNHNH_2$, $[HE + H]^+$ and water, forming a $[CH_2CHNHNHNH_2]\cdot[NH_2NH_2$-$CH_2CH_2OH]^+\cdot H_2O$ structure as shown in Fig. S4 in the ESI.† This structure may also eliminate single and double water as well as $CH_2CHNHNHNH_2 + H_2O$ *via* the following pathways:

$$[CH_2CHNHNHNH_2]\cdot[NH_2NH_2CH_2CH_2OH]^+\cdot H_2O \quad \text{(second probable Structure II)}$$

$$\rightarrow [CH_2CHNHNHNH_2]\cdot[NH_2NH_2CH_2CH_2OH]^+ + H_2O \quad \Delta H = 0.52 \text{ eV} \qquad (3d.2)$$

$$\rightarrow [CH_2CHNHNHNH_2]\cdot[NH_2NH_2CHCH_2]^+ + 2H_2O \quad \Delta H = 1.42 \text{ eV } (\Delta H^{\neq} = 3.25 \text{ eV}) \qquad (3e.2)$$

$$\rightarrow [HE + H]^+ + CH_2CHNHNHNH_2 + H_2O \quad \Delta H = 1.47 \text{ eV} \qquad (3f.2)$$

The third scenario can be characterized by concurrent elimination of a H atom from $[HE + H]^+$ and a $^{\bullet}OH$ radical from HE followed by covalent combination of the remaining fragments, as shown in Fig. S5 in the ESI.† This scenario leads to the formation of the same structure as in the first scenario, *i.e.*, $[HOCH_2CH_2NHNH_2CH_2CH_2NHNH_2]^+\cdot H_2O$ and reactions (3d.1)–(3f.1) may be applied herein.

To determine which structure best describes the experiment, we first fitted the experimental CID thresholds. The cross sections in Fig. 3d and e either miss the rising edge starting from a zero cross section or involve multiple steps and thus are not suitable for LOC fitting. Only the data in Fig. 3f was fitted. It turns out that reaction (3f.2) is in better agreement with the fitted E_0 in Fig. 3f, pinpointing the most probable Structure II as $[CH_2CHNHNHNH_2]\cdot[NH_2NH_2CH_2CH_2OH]^+\cdot H_2O$. The fact that we managed to form $[CH_2CHNHNHNH_2]\cdot[NH_2NH_2CH_2CH_2OH]^+\cdot H_2O$, despite that it being 0.36 eV higher in energy than the conventional Structure I $[HOCH_2CH_2NHNH_2]\cdot[HOCH_2CH_2$-$NH_2NH_2]^+$, demonstrates the importance of secondary cluster reactions. It seems reasonable that Structure II most likely formed within the desolvation capillary by a 3-body process and only survived the soft in-source collisions. We note that Structure II does not affect the dominance of Structure I, as Structure I has an order of magnitude higher abundance than Structure II. This prompted us to focus more on the dominating cluster structures for the remaining larger cluster ions wherein structural complexity and variety increased.

$[(HE)_3 + H]^+$ (m/z 229). This cluster ion can eliminate one and two HE, producing $[(HE)_2 + H]^+$ and $[HE + H]^+$, respectively. A representative product ion mass spectrum and individual product cross sections are reported in Fig. 4. Patrick *et al.*[33] reported the most stable structures for $[(HE)_3 + H]^+$, $[(HEHN)HE + H]^+$, $[(HEHN)_2HE + H]^+$ and $[(HEHN)(HE)_2 + H]^+$ by using classical all-atom force fields to generate initial-guess geometries followed by using the M06-2X/6-311++G(d,p) functional to identify global minima. We adopted these cluster structures and re-optimized

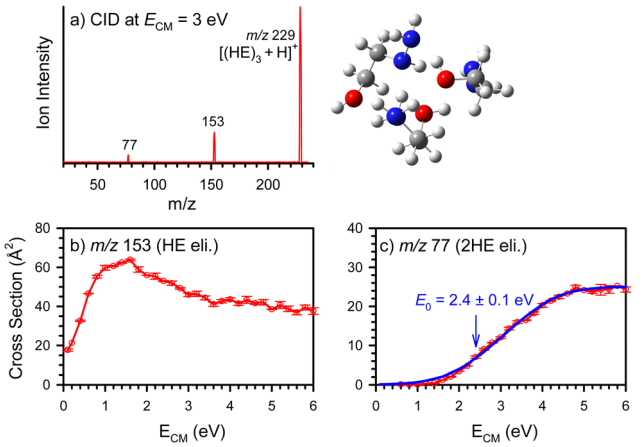

Fig. 4 (a) Structure and a representative CID product ion mass spectrum of $[(HE)_3 + H]^+$; and (b and c) individual product ion cross sections as a function of E_{CM}, wherein red lines with error bars represent the experimental data and blue line represents the LOC fit.

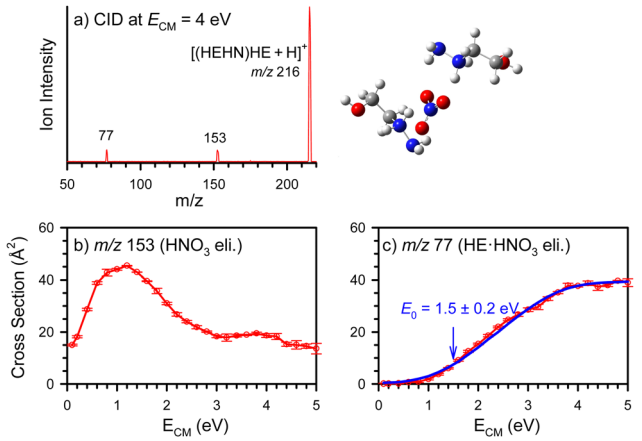

Fig. 5 (a) Structure and a representative CID product ion mass spectrum of $[(HEHN)HE + H]^+$; and (b and c) individual product ion cross sections as a function of E_{CM}, wherein red lines with error bars represent the experiment and blue line represents the LOC fit.

them at the ωB97XD/6-31+G(d,p) level of theory. The optimized $[(HE)_3 + H]^+$ structure is shown in Fig. 4.

Using this as the starting reactant structure, we have obtained the following reaction energetics:

$$[(HE)_3 + H]^+$$

$$\rightarrow [(HE)_2 + H]^+ + HE \quad \Delta H = 1.05 \text{ eV} \tag{4b}$$

$$\rightarrow [HE + H]^+ + 2HE \quad \Delta H = 2.44 \text{ eV} \tag{4c}$$

Due to the low reaction threshold of single HE elimination, the cross section has exceeded zero even at the lowest E_{CM}. As a result, we were not able to observe a complete threshold profile (*i.e.*, rising from a zero-cross section) at low E_{CM} range which was required for a quantitative LOC fitting. However, a test LOC fitting verified that the E_0 value should be no more than the theoretical value of 1.07 eV. On the other hand, the LOC fitting was able to reproduce the cross section for double HE elimination. The fact that the LOC-deduced E_0 value closely matches the calculated product ΔH in reaction (4c) indicates that the dissociation has no reverse activation barrier, *i.e.*, the barrier is located at the dissociation product asymptote. This is not surprising as the cluster ions are bonded by ion–dipole interaction and H-bonds, and there is no centrifugal barrier for dissociation.[103] The decrease in the single HE elimination cross section at high E_{CM} is due to the inter-channel competition between single- and double-HE elimination.

4.3 Dissociation of $[(HEHN)_nHE + H]^+$ (n = 1, 2)

$[(HEHN)HE + H]^+$ (m/z 216). $[(HEHN)HE + H]^+$ may eliminate HNO_3 (an indicator for intra-ion pair proton transfer in HEHN) and HEHN, as shown in Fig. 5a. Note that the product HEHN remains as an ion pair when it is dissociating from the parent ion (Fig. S1, ESI†); but it would ultimately convert to a stable H-bonded neutral structure at the product asymptote. Therefore, it is presented as HE·HNO_3 in dissociation products. Using the $[(HEHN)HE + H]^+$ structure reported by Patrick *et al.*,[33] its dissociation enthalpies were calculated as:

$$[(HEHN)HE + H]^+$$

$$\rightarrow [(HE)_2 + H]^+ + HNO_3 \quad \Delta H = 0.82 \text{ eV} \tag{5b}$$

$$\rightarrow [HE + H]^+ + HE{\cdot}HNO_3 \quad \Delta H = 1.42 \text{ eV} \tag{5c}$$

As shown in Fig. 5b, the dissociation threshold for HNO_3 elimination is rather low so the cross section has already become non-zero at the lowest E_{CM}. The is consistent with the calculated ΔH (0.82 eV) of reaction (5b). It implies that the proton transfer within the activated cluster ion has an insignificant or no activation barrier. The cross section for HNO_3 elimination presents significant decrease above E_{CM} = 1.5 eV, which is due to the competition with the increasing HE·HNO_3 elimination at higher energies. The LOC fitting for the HE·HNO_3 elimination cross section (Fig. 5c) has fully reproduced the experimental E_{CM} dependence, and the E_0 value extracted from the fitting (E_0 = 1.5 ± 0.2 eV) matches the theoretical dissociation energy (ΔH = 1.42 eV).

$[(HEHN)_2HE + H]^+$ (m/z 355). The CID of $[(HEHN)_2HE + H]^+$ mimics that of $[(HEHN)HE + H]^+$ in terms of HNO_3 and HE·HNO_3 elimination, and the elimination of two HNO_3 or two HE·HNO_3 becomes feasible for $[(HEHN)_2HE + H]^+$ as shown in Fig. 6. These products are the same to what were reported by Patrick *et al.*[33] The cross sections for single and double HNO_3 elimination (Fig. 6b and c, respectively) start to drop at or before reaching their theoretical dissociation thresholds, which has prohibited LOC fitting. We fit the cross sections for the remaining three product channels in Fig. 6d–f. The resulting E_0 values are consistent with the calculated ΔHs for reactions (6d)–(6f). The CID of $[(HEHN)_2HE + H]^+$ is dominated by elimination of (HE·HNO_3 + HNO_3) at E_{CM} above 2.5 eV, switching to double HE·HNO_3 elimination above 7 eV. The fact that HNO_3 elimination becomes less competitive than HE·HNO_3

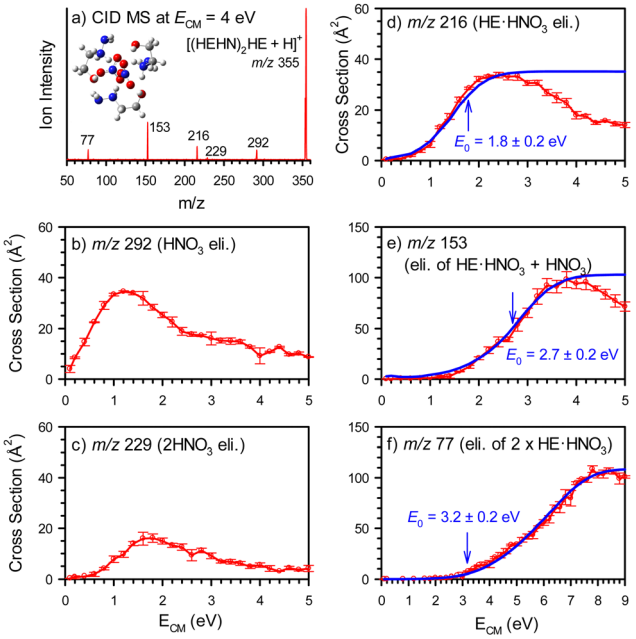

Fig. 6 (a) Structure and a representative CID product ion mass spectrum of [(HEHN)$_2$HE + H]$^+$; and (b–f) individual product ion cross sections as a function of E_{CM}, wherein red lines with error bars represent the experimental data and blue lines represent the LOC fits.

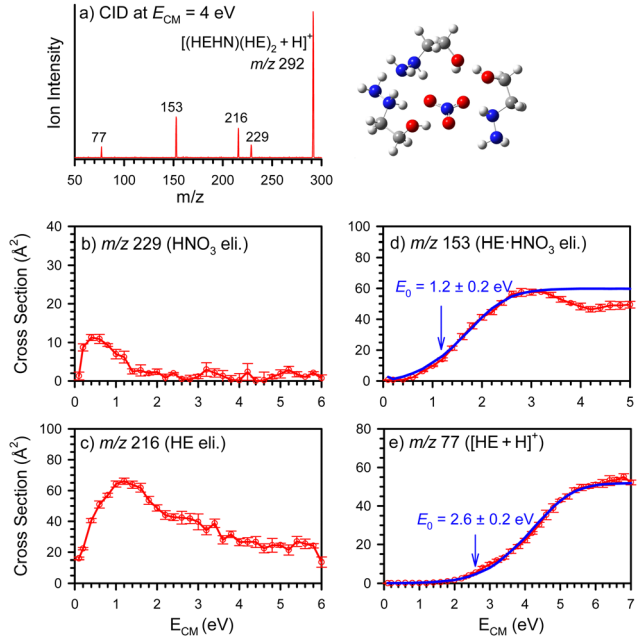

Fig. 7 (a) Structure and a representative CID product ion mass spectrum of [(HEHN)(HE)$_2$ + H]$^+$; and (b–e) individual product ion cross sections as a function of E_{CM}, wherein red lines with error bars represent the experiment and blue lines represent the LOC fits.

elimination above 2 eV implies that the proton transfer reaction (leading to formation of HNO_3) within HEHN is less favored at higher energies.

$$[(HEHN)_2HE + H]^+$$

$$\rightarrow [(HEHN)(HE)_2 + H]^+ + HNO_3 \quad \Delta H = 1.42 \text{ eV} \quad (6b)$$

$$\rightarrow [(HE)_3 + H]^+ + 2HNO_3 \quad \Delta H = 2.26 \text{ eV} \quad (6c)$$

$$\rightarrow [(HEHN)HE + H]^+ + HE{\cdot}HNO_3 \quad \Delta H = 1.70 \text{ eV} \quad (6d)$$

$$\rightarrow [(HE)_2 + H]^+ + HE{\cdot}HNO_3 + HNO_3 \quad \Delta H = 2.52 \text{ eV} \quad (6e)$$

$$\rightarrow [HE + H]^+ + 2[HE{\cdot}HNO_3] \quad \Delta H = 3.12 \text{ eV} \quad (6f)$$

4.4 Dissociation of $[(HEHN)_n(HE)_2 + H]^+$ (n =1, 2)

$[(HEHN)(HE)_2 + H]^+$ (m/z 292). This cluster may eliminate HNO_3, HE, HE·HNO_3 or the $[HE + H]^+$ ion (accompanied with the elimination of HE·HNO_3 + HE). The E_{CM}-dependence for the HNO_3 elimination is reminiscent of reactions (6b) and (6c) for $[(HEHN)_2HE + H]^+$, *i.e.*, the cross section drops before approaching the nominal dissociation threshold. This reaffirms that HNO_3 elimination is less competitive with others above $E_{CM} > 3.0$ eV even though it has the lowest threshold (0.81 eV for reaction (7b)). The lowest-energy structure for $[(HEHN)(HE)_2 + H]^+$ (in Fig. 7a) was adopted from the work of Patrick *et al.*[33] The LOC fits for the HE·HNO_3 and HE·HNO_3 + HE elimination (Fig. 7d and e) have reproduced their cross sections and supported the calculated products' ΔH. The HE elimination dominates the CID from the lowest E_{CM} to 2 eV, the HE·HNO_3 elimination dominates from 2 to 5 eV, and the $[HE + H]^+$ elimination dominates above 5 eV.

$$[(HEHN)(HE)_2 + H]^+$$

$$\rightarrow [(HE)_3 + H]^+ + HNO_3 \quad \Delta H = 0.83 \text{ eV} \quad (7b)$$

$$\rightarrow [(HEHN)HE + H]^+ + HE \quad \Delta H = 1.06 \text{ eV} \quad (7c)$$

$$\rightarrow [(HE)_2 + H]^+ + HE{\cdot}HNO_3 \quad \Delta H = 1.09 \text{ eV} \quad (7d)$$

$$\rightarrow [HE + H]^+ + HE{\cdot}HNO_3 + HE \quad \Delta H = 2.48 \text{ eV} \quad (7e)$$

$[(HEHN)_2(HE)_2 + H]^+$ (m/z 431). Fig. 8 presents the CID results and LOC fits for the largest cluster, $[(HEHN)_2(HE)_2 + H]^+$, measured in the experiment. Its fragmentation is featured by the elimination of HE and HE·HNO_3; but no HNO_3 elimination was observed. To identify the lowest-energy reactant structure, multiple candidate structures were created by using classical molecular mechanics simulations. These candidate structures were subjected to geometry optimization using the ωB97XD level of theory with the basis set increased from 3-21G, through 6-31+G(d) and to 6-31+G(d,p). Fig. S6 in the ESI,† illustrates the converged structures within an energy range of 0.3 eV, of which the global minimum conformer has a population of 81%.

The global minimum structure was then used as the starting reactant ion to calculate thresholds in reactions (8b)–(8e). Overall, the calculated energetics agrees with the experiment within the combined experimental and theoretical uncertainties. This suggests that the reactant structure shown in Fig. 8a was detected. The less ideal LOC fits in Fig. 8 may be due to

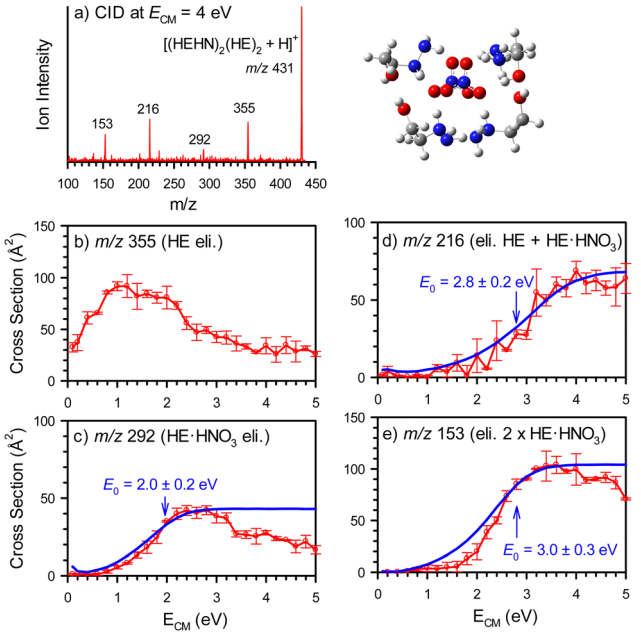

Fig. 8 (a) Structure and a representative CID product ion mass spectrum of $[(HEHN)_2(HE)_2 + H]^+$; and (b–e) individual product ion cross sections as a function of E_{CM}, wherein red lines with error bars represent the experimental data and blue lines represent the LOC fits.

contributions from low-population reactant conformers and secondary dissociation products in the experiment.

$$[(HEHN)_2(HE)_2 + H]^+$$

$$\rightarrow [(HEHN)_2HE + H]^+ + HE \quad \Delta H = 1.16 \text{ eV} \quad (8b)$$

$$\rightarrow [(HEHN)(HE)_2 + H]^+ + HE{\cdot}HNO_3 \quad \Delta H = 1.82 \text{ eV} \quad (8c)$$

$$\rightarrow [(HEHN)HE + H]^+ + HE{\cdot}HNO_3 + HE \quad \Delta H = 3.00 \text{ eV} \quad (8d)$$

$$\rightarrow [(HE)_2 + H]^+ + 2[HE{\cdot}HNO_3] \quad \Delta H = 3.20 \text{ eV} \quad (8e)$$

4.5 Dissociation of $[(HE)_nC_2H_4OH]^+$ (n = 1, 2)

$[(HE)C_2H_4OH]^+$ (m/z 121). The $[(HE)_nC_2H_4OH]^+$ series was not reported in the literature, except for $C_2H_4OH^+$.[14] The CID of $[(HE)C_2H_4OH]^+$ shows only water elimination with a relatively low threshold energy, as shown in Fig. 9. No $[HE + H]^+$ or $C_2H_4OH^+$ was observed, ruling out the possibility of a H-bonded $HE{\cdot}C_2H_4OH^+$ or $[HE + H]^+{\cdot}C_2H_3OH$ structure for m/z 121.

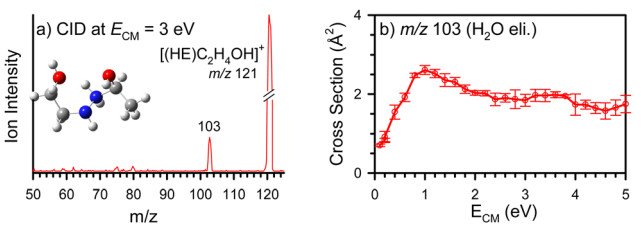

Fig. 9 (a) Structure and a representative CID product ion mass spectrum of $[(HE)C_2H_4OH]^+$; and (b) product ion cross sections as a function of E_{CM}.

To explore the structures of m/z 121 that may contain new covalent structures, quasi-classical direct dynamics simulations were carried out to mimic complex formation from the possible constituents in m/z 121. Note that an isolated $C_2H_4OH^+$ (2-hydroxyethyl cation) would convert to a CH_3CHOH^+ (1-hydoxyethylium) structure in the gas phase. For this reason, we simulated the bimolecular collisions of $[HE + H]^+$ + neural CH_2CHOH and of HE + CH_3CHOH^+ cation. For collisions of $[HE + H]^+$ + CH_2CHOH, no complex formation or other reactions were observed. On the contrary, the collisions of HE + CH_3CHOH^+ led to two covalent structures $[HOCH_2CH_2NHNH_2CH(OH)CH_3]^+$ and $[HOCH_2CH_2NH(NH_2)CH(OH)CH_3]^+$ (wherein the protonated carbonyl group in CH_3CHOH^+ attacks and binds to the N-terminus and secondary amine in HE, respectively). The formation yields for the first structure are 4% at b = 0 Å, 6% at 1.5 Å and 3% at 3.0 Å, and the yields for the second structure are 3% at 0 Å, 2% at 1.5 Å and 2% at 3.0 Å. No strong b-dependence was observed for either reaction, which is consistent with complex formation in reactive collisions. $[HOCH_2CH_2NHNH_2CH(OH)CH_3]^+$ not only has a higher trajectory formation yield but also lies at an energy 0.11 eV below $[HOCH_2CH_2NH(NH_2)CH(OH)CH_3]^+$.

Yet, neither of the two structures has a H-bonded water which is required to rationalize the low CID threshold in Fig. 9b. However, $[HOCH_2CH_2NHNH_2CH(OH)CH_3]^+$ may interconvert to a H-bonded structure $[HOCH_2CH_2NHNHCHCH_3]^+{\cdot}H_2O$ *via* a barrier of 0.79 eV, and the latter is featured by a low-energy (0.54 eV) water-elimination channel, as depicted in Fig. S7 in the ESI.† A similar interconversion pathway was identified, leading from $[HOCH_2CH_2NH(NH_2)CH(OH)CH_3]^+$ to $[HOCH_2CH_2N(NH_2)CHCH_3]^+{\cdot}H_2O$ *via* a barrier of 1.78 eV, as shown in Fig. S8 in the ESI.† $[HOCH_2CH_2N(NH_2)CHCH_3]^+{\cdot}H_2O$ may also lose a water with a threshold energy of 0.41 eV. Based on these results, it is reasonable to propose $[HOCH_2CH_2NHNHCHCH_3]^+{\cdot}H_2O$ and $[HOCH_2CH_2N(NH_2)CHCH_3]^+{\cdot}H_2O$ as the two probable structures for m/z 121, with the first one being more favorable. The dissociation energetics in reactions (9b.1) and (9b.2) match the low-threshold dissociation observed in Fig. 9b.

$$[HOCH_2CH_2NHNHCHCH_3]^+{\cdot}H_2O$$

$$\rightarrow [HOCH_2CH_2NHNHCHCH_3]^+ + H_2O \quad \Delta H = 0.52 \text{ eV} \quad (9b.1)$$

$$[HOCH_2CH_2N(NH_2)CHCH_3]^+{\cdot}H_2O$$

$$\rightarrow [HOCH_2CH_2N(NH_2)CHCH_3]^+ + H_2O \quad \Delta H = 0.41 \text{ eV} \quad (9b.2)$$

$[(HE)_2C_2H_4OH]^+$ (m/z 197). The structures for m/z 197 were calculated by adding a HE to different positions in $[HOCH_2CH_2NHNH_2CH(OH)CH_3]^+$ and with different orientations, followed by optimizing geometries at the ωB97XD/6-31+G(d,p) level of theory. Stable $[HE][HOCH_2CH_2NHNH_2CH(OH)CH_3]^+$ conformers are summarized in Fig. S9 in the ESI.† Fig. S10 in the ESI,† shows the formation of a water-bonded structure $[HE][HOCH_2CH_2NHNHCHCH_3]^+{\cdot}H_2O$ from

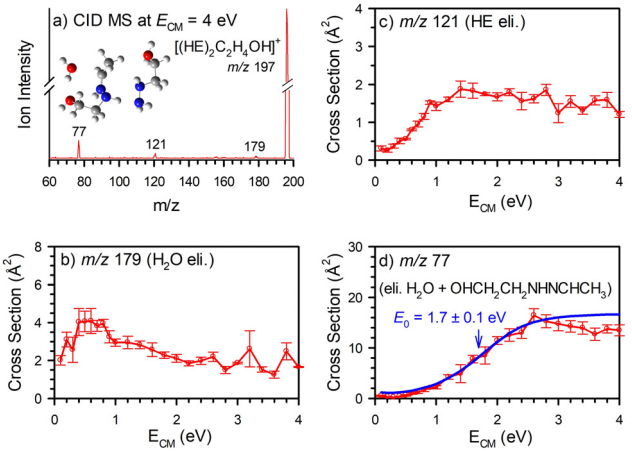

Fig. 10 (a) Structure and a representative CID product ion mass spectrum of $[(HE)_2C_2H_4OH]^+$; and (b–d) individual product ion cross sections as a function of E_{CM}, wherein red lines with error bars represent the experimental data and blue line represents the LOC fit.

the lowest-energy conformer $[HE][HOCH_2CH_2NHNH_2CH(OH)CH_3]^+$ *via* an in-source reaction. $[HE][HOCH_2CH_2NHNHCHCH_3]^+\cdot H_2O$ has water elimination opening at 0.32 eV (reaction (10b)), HE elimination at 0.79 eV (reaction (10c)), and concurrent loss of $HOCH_2CH_2NHNCHCH_3$ + H_2O at 1.61 eV (reaction (10d), occurring after a barrierless proton transfer from $[HOCH_2CH_2$-$NHNHCHCH_3]^+$ to HE). These dissociation energies agree with the CID of *m*/*z* 197 (Fig. 10) and suggest $[HE][HOCH_2$-$CH_2NHNHCHCH_3]^+\cdot H_2O$ as the major reactant structure. The $[HE][HOCH_2CH_2NHNH_2CHCH_3]^+$ itself may contribute to the CID but cannot be significant as it has a higher ΔH (1.87 eV, see Fig. S10, ESI†) for producing $[HE + H]^+$ than the experiment (1.7 eV). Although it could be possible, we did not investigate a structure for *m*/*z* 197 that may form upon the addition of HE to $[HOCH_2CH_2N(NH_2)CHCH_3]^+\cdot H_2O$. The rationalization is that there is no proton available from $[HOCH_2CH_2N(NH_2)CHCH_3]^+\cdot H_2O$ to produce a $[HE + H]^+$ product.

$$[HE][HOCH_2CH_2NHNHCHCH_3]^+\cdot H_2O$$

$$\rightarrow [HE][HOCH_2CH_2NHNHCHCH_3]^+ + H_2O \quad \Delta H = 0.29 \text{ eV} \qquad (10b)$$

$$\rightarrow [HOCH_2CH_2NHNHCHCH_3]^+\cdot H_2O + HE \quad \Delta H = 0.81 \text{ eV} \qquad (10c)$$

$$\rightarrow [HE + H]^+ + HOCH_2CH_2NHNCHCH_3 + H_2O \quad \Delta H = 1.61 \text{ eV} \qquad (10d)$$

5 General trends in cluster dissociation

The CID data in this work has served two purposes: first, the experimental dissociation energies were used to compare with the thermodynamics of the proposed cluster structures, from which the most probable cluster ion structures were identified, their fragmentation product pathways, branching and major products were analyzed, and accurate thermodynamic data were accumulated; second, despite that CID with Xe atoms would not occur in the space environment, fragmentation of cluster ions indeed happens substantially in the spacecraft propulsion system as aforementioned in Introduction and affects the propulsion efficiency. In this context, the cluster post-activation and fragmentation information and gas-phase cluster ion chemistry learned from Xe-CID can be extrapolated to the thruster system in space, and provide insight into the ultimate fate of the species ejected from the thruster.

The present work has shown that each cluster ion is able to present multiple dissociation pathways, partly due to the protic nature of HEHN. Scheme 1 outlines in a flowchart both primary and secondary dissociation channels, and Table 1 summarizes their major product ions and complementary neutral losses and corresponding dissociation thresholds. Common features and general trends may be revealed from the examination of Scheme 1 and Table 1 as follows: (1) water elimination is expected from H-bonded water complexes, which have low dissociation thresholds, except for $[HE + H]^+$, wherein the water is eliminated from a covalent structure; (2) HNO_3 elimination (*i.e.*, proton transfer-mediated dissociation) is most facile in $[(HEHN)_{1-2}HE + H]^+$. It becomes less kinetically favorable in large clusters as the NO_3^- anions are encapsulated within a large assembly and surrounded by cations; (3) large cluster ions tend to eliminate HE and/or HE·HNO_3 moieties; (4) for large HEHN clusters, the fragment ions still contain the $[(HE)_{n+1} + H]^+$ and $[(HEHN)_nHE + H]^+$ constituents. The implication is that

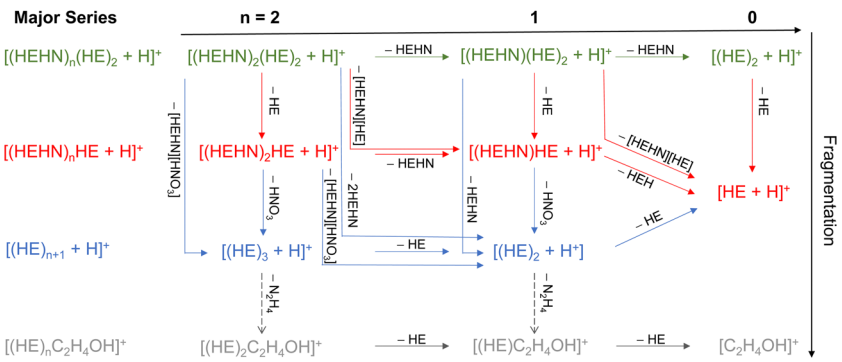

Scheme 1 Formation and fragmentation pathways of positively charged HEHN clusters and derivatives. The four major series of ionic species are distinguished by the colors of their labels, and neutral fragments are labeled in black.

Table 1 Major dissociation pathways and threshold energies (ΔH, 0 K) for HEHN positive cluster ions

Cluster ions	ΔH (eV)	Fragment ion	Complementary neutral
$[HE + H]^+$	0.10 (1.93[a])	$[CH_3CH{=}NHNH_2]^+$	H_2O
$[(HE)_2 + H]^+$ (Structure I for m/z 153)	1.39	$[HE + H]^+$	HE
$[CH_2CHNHNH_2][NH_2NH_2CH_2CH_2OH]^+{\cdot}H_2O$	0.52	$[CH_2CHNHNH_2]{\cdot}[NH_2NH_2CH_2CH_2OH]^+$	H_2O
(Structure II for m/z 153)	1.47	$[HE + H]^+$	$CH_2CHNHNH_2 + H_2O$
$[(HE)_3 + H]^+$	1.05	$[(HE)_2 + H]^+$	HE
$[(HEHN)HE + H]^+$	0.82	$[(HE)_2 + H]^+$	HNO_3
	1.42	$[HE + H]^+$	$HE{\cdot}HNO_3$
$[(HEHN)_2HE + H]^+$	2.52	$[(HE)_2 + H]^+$	$HE{\cdot}HNO_3 + HNO_3$
	3.12	$[HE + H]^+$	$2HE{\cdot}HNO_3$
$[(HEHN)(HE)_2 + H]^+$	1.06	$[(HEHN)HE + H]^+$	HE
	1.09	$[(HE)_2 + H]^+$	$HE{\cdot}HNO_3$
$[(HEHN)_2(HE)_2 + H]^+$	1.16	$[(HEHN)_2HE + H]^+$	HE
	3.20	$[(HE)_2 + H]^+$	$HE{\cdot}HNO_3$
$[HOCH_2CH_2NHNHCHCH_3]^+{\cdot}H_2O$ (m/z 121)	0.52	$[HOCH_2CH_2NHNHCHCH_3]^+$	H_2O
$[HOCH_2CH_2N(NH_2)CHCH_3]^+{\cdot}H_2O$ (another structure for m/z 121)	0.41	$[HOCH_2CH_2N(NH_2)CHCH_3]^+$	H_2O
$[HE][HOCH_2CH_2NHNHCHCH_3]^+{\cdot}H_2O$	1.61	$[HE + H]^+$	$HOCH_2CH_2NHNCHCH_3 + H_2O$

[a] Activation energy for dissociation.

fragmentation promotes the formation of smaller (and lower mass) HE and/or HEHN cluster ions, which may increase specific impulse; and (5) energetically, all cluster ions have the first dissociation channel open at an threshold energy of $\leq$1.6 eV, and many of which are below 1 eV.

6 Conclusions

This work has combined mass spectrometric study on the dissociation of $[(HEHN)_nHE + H]^+$, $[(HEHN)_n(HE)_2 + H]^+$, $[(HE)_{n+1} + H]^+$ and $[(HE)_nC_2H_4OH]^+$ (n = 0–2) cluster ions formed in positive electrospray with theoretical investigation of cluster structures to understand the reaction dynamics as well as pathways to product formation. The focus was on exploring what constituents are to be expected in the electrospray of HEHN ionic liquid, the stability and structures of the clusters, what fragmentation reactions happen upon post-source activation, and how well the theory can reproduce the experiment. All HEHN cluster ions are prone to fragmentation. $[(HE)_{1-2} + H]^+$ accounts for the most abundant compositions in the electrospray plume and has the lowest m/z. $[HE + H]^+$ and $[(HEHN)HE + H]^+$ represent the most common fragment ions from larger cluster ions, while HE, $HE{\cdot}HNO_3$ and HNO_3 represent the complementary neutral fragments. H-bonded water was detected in $[CH_2CHNHNH_2]{\cdot}[NH_2NH_2CH_2CH_2OH]^+{\cdot}H_2O$, $[HOCH_2CH_2NHNHCHCH_3]^+{\cdot}H_2O$, $[HOCH_2CH_2N(NH_2)CHCH_3]^+{\cdot}H_2O$ and $[HE][HOCH_2CH_2NHNHCHCH_3]^+{\cdot}H_2O$, each of which has a characteristic low-energy water elimination channel. These clusters, especially the water-bonded ones, may not necessarily form in other electrospray methods. These results are of importance for modeling spacecraft electrospray thruster performance, in particular, small ions resulting from cluster fragmentation can help improve specific impulse in electrospray thrusters.

Conflicts of interest

There are no conflicts to declare.

Acknowledgements

J. L. and W. Z. acknowledge the support by the Air Force Research Laboratory through Jacobs Technology Inc. (Subcontract number RAPT1-0000001672). S. D. C. acknowledges support from the Air Force Office of Scientific Research under award number FA9300-20-F-9801.

References

1 D. R. MacFarlane and K. R. Seddon, *Aust. J. Chem.*, 2007, **60**, 3–5.
2 D. R. MacFarlane, M. Kar and J. M. Pringle, *Fundamentals of Ionic Liquids: From Chemistry to Applications*, Wiley-VCH Verlag GmbH & Co. KGaA, Weinheim, Germany, 2017.
3 T. Welton, *Chem. Rev.*, 1999, **99**, 2071–2083.
4 J. P. Hallett and T. Welton, *Chem. Rev.*, 2011, **111**, 3508–3576.
5 A. Avid, J. L. Ochoa, Y. Huang, Y. Liu, P. Atanassov and I. V. Zenyuk, *Nat. Comm.*, 2022, **13**, 6349.
6 H. Qi, Y. Ren, S. Guo, Y. Wang, S. Li, Y. Hu and F. Yan, *ACS Appl. Mater. Interfaces*, 2020, **12**, 591–600.
7 S. Schneider, T. Hawkins, M. Rosander, G. Vaghjiani, S. Chambreau and G. Drake, *Energy Fuels*, 2008, **22**, 2871–2872.
8 Y. Zhang, H. Gao, Y.-H. Joo and J. M. Shreeve, *Angew. Chem., Int. Ed.*, 2011, **50**, 9554–9562.
9 Q. Zhang and J. M. Shreeve, *Chem. Rev.*, 2014, **114**, 10527–10574.
10 P. D. McCrary, G. Chatel, S. A. Alaniz, O. A. Cojocaru, P. A. Beasley, L. A. Flores, S. P. Kelley, P. S. Barber and R. D. Rogers, *Energy Fuels*, 2014, **28**, 3460–3473.
11 S. R. Jain, *J. Indian Inst. Sci.*, 1989, **69**, 175–191.
12 I. Romero-Sanz, R. Bocanegra, J. Fernandez de la Mora and M. Gamero-Castano, *J. Appl. Phys.*, 2003, **94**, 3599–3605.
13 Y.-h Chiu and R. A. Dressler, *Ionic Liquids IV (ACS Symp. Ser.)*, American Chemical Society, 2007, vol. 975, pp. 138–160.

14 B. D. Prince, B. A. Fritz and Y.-H. Chiu, *Ionic liquids: Science and Applications (ACS Symp. Ser.)*, American Chemical Society, 2012, vol. 1117, pp. 27–49.
15 S. P. Berg, J. Rovey, B. Prince, S. Miller and R. Bemish, 51st AIAA/SAE/ASEE Joint Propulsion Conference, Orlando, FL, 2015.
16 F. Mier-Hicks and P. C. Lozano, *J. Propul. Power*, 2017, **33**, 456–467.
17 B. D. Prince, C. J. Annesley, R. J. Bemish and S. Hunt, *AIAA Propulsion and Energy 2019 Forum*, Indianapolis, IN, 2019.
18 B. R. Donius and J. L. Rovey, *J. Spacecraft Rockets*, 2011, **48**, 110–123.
19 J. Rovey, C. T. Lyne, A. J. Mundahl, N. Rasmont, M. S. Glascock, M. J. Wainwright and S. P. Berg, *AIAA Propulsion and Energy 2019 Forum*, Indianapolis, IN, 2019.
20 S. Schneider, T. Hawkins, Y. Ahmed, S. Deplazes and J. Mills, *Ionic Liquids: Science and Applications (ACS Symp. Ser.)*, American Chemical Society, 2012, vol. 1117, pp. 1–25.
21 S. V. Stovbun, A. N. Shchegolikhin, S. V. Usachev, S. V. Khomik and S. P. Medvedev, *Acta Astronaut.*, 2017, **135**, 110–113.
22 T. L. Greaves and C. J. Drummond, *Chem. Rev.*, 2015, **115**, 11379–11448.
23 J. L. Shamshina, M. Smiglak, D. M. Drab, T. G. Parker, H. W. H. Dykes, Jr., R. Di Salvo, A. J. Reich and R. D. Rogers, *Chem. Commun.*, 2010, **46**, 8965–8967.
24 T. W. Hawkins, A. J. Brand and G. W. Drake, *US Pat.*, 20140190598, 2014.
25 A. Chowdhury and S. T. Thynell, *Propellants, Explos., Pyrotech.*, 2010, **35**, 572–581.
26 A. A. Esparza, S. D. Chambreau, G. L. Vaghjiani and E. Shafirovich, *Combust. Flame*, 2020, **220**, 1–6.
27 S. D. Chambreau, D. M. Popolan-Vaida, O. Kostko, J. K. Lee, Z. Zhou, T. A. Brown, P. Jones, K. Shao, J. Zhang, G. L. Vaghjiani, R. N. Zare and S. R. Leone, *J. Phys. Chem. A*, 2022, **126**, 373–394.
28 D. W. Kohn, H. Clauberg and P. Chen, *Rev. Sci. Instrum.*, 1992, **63**, 4003–4005.
29 S. D. Chambreau, D. M. Popolan-Vaida, G. L. Vaghjiani and S. R. Leone, *J. Phys. Chem. Lett.*, 2017, **8**, 2126–2130.
30 S. D. Chambreau, C. J. Koh, D. M. Popolan-Vaida, C. J. Gallegos, J. B. Hooper, D. Bedrov, G. L. Vaghjiani and S. R. Leone, *J. Phys. Chem. A*, 2016, **120**, 8011–8023.
31 Z. Zhou, J. K. Lee, S. C. Kim and R. N. Zare, *Anal. Chem.*, 2016, **88**, 5542–5548.
32 J. K. Lee, E. T. Jansson, H. G. Nam and R. N. Zare, *Anal. Chem.*, 2016, **88**, 5453–5461.
33 A. L. Patrick, K. M. Vogelhuber, B. D. Prince and C. J. Annesley, *J. Phys. Chem. A*, 2018, **122**, 1960–1966.
34 H. J. Zeng, T. Khuu, S. D. Chambreau, J. A. Boatz, G. L. Vaghjiani and M. A. Johnson, *J. Phys. Chem. A*, 2020, **124**, 10507–10516.
35 P. Lozano and M. Martinez-Sanchez, 41st AIAA/ASME/SAE/ASEE Joint Propulsion Conference & Exhibit, Tucson, Arizona, 2005.
36 P. Lozano and M. Martínez-Sánchez, *J. Colloid Interface Sci.*, 2005, **282**, 415–421.
37 B. Ticknor, S. Miller and Y.-H. Chiu, 45th AIAA/ASME/SAE/ASEE Joint Propulsion Conference & Exhibit, Denver, Coloradp, 2009.
38 M. Gamero-CastaÑO, *J. Fluid Mech.*, 2010, **662**, 493–513.
39 T. M. Coles and P. C. Lozano, 49th AIAA/ASME/SAE/ASEE Joint Propulsion Conference, San Jose, CA, 2013.
40 C. Miller and P. C. Lozano, 52nd AIAA/SAE/ASEE Joint Propulsion Conference, Salt Lake City, UT, 2016.
41 S. W. Miller, B. D. Prince, R. J. Bemish and J. Rovey, 52nd AIAA/SAE/ASEE Joint Propulsion Conference, Salt Lake City, UT, 2016.
42 M. Breddan, A. Collins and R. Wirz, The 36th International Electric Propulsion Conference, Vienna, Austria, 2019.
43 M. J. Wainwright, J. L. Rovey, S. W. Miller, B. D. Prince and S. P. Berg, *J. Propul. Power*, 2019, **35**, 922–929.
44 A. L. Patrick, *Rapid Commun. Mass Spectrom.*, 2020, **34**, e8587.
45 N. M. Uchizono, A. L. Collins, A. Thuppul, P. L. Wright, D. Q. Eckhardt, J. Ziemer and R. E. Wirz, *Aerospace*, 2020, **7**, 141.
46 N. M. Uchizono, A. L. Collins, C. Marrese-Reading, S. M. Arestie, J. K. Ziemer and R. E. Wirz, *J. Appl. Phys.*, 2021, **130**, 143301.
47 N. M. Uchizono, C. Marrese-Reading, S. M. Arestie, A. L. Collins, J. K. Ziemer and R. E. Wirz, *Appl. Phys. Lett.*, 2022, **121**, 074103.
48 J. Fernández de la Mora, *J. Fluid Mech.*, 1992, **243**, 561–574.
49 J. Plante and B. Lee, Environmental Conditions for Space Flight Hardware: A Survey, NASA Electronic Parts and Packaging (NEPP) Program, 2004.
50 M. Gamero-Castano, *Phys. Rev. E*, 2019, **99**, 061101.
51 J. M. Crowley, *J. Appl. Phys.*, 1977, **48**, 145–147.
52 S. C. Nanita and R. G. Cooks, *Angew. Chem., Int. Ed.*, 2006, **45**, 554–569.
53 J. Zhang, B. Bogdanov, A. Parkins and C. M. McCallum, *J. Phys. Chem. A*, 2020, **124**, 3535–3541.
54 L. Konermann and Y. Haidar, *Anal. Chem.*, 2022, **94**, 16491–16501.
55 D. A. Bonhommeau, R. Spezia and M.-P. Gaigeot, *J. Chem. Phys.*, 2012, **136**, 184503.
56 P. C. Lozano, *J. Phys. D: Appl. Phys.*, 2006, **39**, 126–134.
57 W. Zhou, J. Liu, S. D. Chambreau and G. L. Vaghjiani, *Phys. Chem. Chem. Phys.*, 2022, **24**, 14033–14043.
58 Y. Fang and J. Liu, *J. Phys. Chem. A*, 2009, **113**, 11250–11261.
59 in *State-selected and state-to-state ion-molecule reaction dynamics. Part 1: Experiment*, ed. C.-Y. Ng and M. Baer, Wiley Interscience, New York, 1992.
60 P. B. Armentrout, *Int. J. Mass Spectrom.*, 2000, **200**, 219–241.
61 P. B. Armentrout, *J. Anal. At. Spectrom.*, 2004, **19**, 571–580.
62 S. K. Chowdhury, V. Katta and B. T. Chait, *Rapid Commun. Mass Spectrom.*, 1990, **4**, 81–87.
63 T. Kim, K. Tang, H. R. Udseth and R. D. Smith, *Anal. Chem.*, 2001, **73**, 4162–4170.

64 K. Tang, A. V. Tolmachev, E. Nikolaev, R. Zhang, M. E. Belov, H. R. Udseth and R. D. Smith, *Anal. Chem.*, 2002, **74**, 5431–5437.

65 R. M. Moision and P. B. Armentrout, *J. Am. Soc. Mass Spectrom.*, 2007, **18**, 1124–1134.

66 A. N. Krutchinsky, I. V. Chernushevich, V. L. Spicer, W. Ens and K. G. Standing, *J. Am. Soc. Mass Spectrom.*, 1998, **9**, 569–579.

67 D. J. Douglas and J. B. French, *J. Am. Mass Spectrom.*, 1992, **3**, 398–408.

68 R. D. Levine and R. B. Bernstein, *Molecular Reaction Dynamics and Chemical Reactivity*, Oxford University Press, New York, 1987.

69 C. Rebick and R. D. Levine, *J. Chem. Phys.*, 1973, **58**, 3942–3952.

70 J. Liu, B. van Devener and S. L. Anderson, *J. Chem. Phys.*, 2002, **116**, 5530–5543.

71 M. M. Moe, J. Benny, Y. Sun and J. Liu, *Phys. Chem. Chem. Phys.*, 2021, **23**, 9365–9380.

72 M. B. Sowa-Resat, P. A. Hintz and S. L. Anderson, *J. Phys. Chem.*, 1995, **99**, 10736–10741.

73 Y. Sun, M. M. Moe and J. Liu, *Phys. Chem. Chem. Phys.*, 2020, **20**, 14875–14888.

74 M. T. Rodgers, K. M. Ervin and P. B. Armentrout, *J. Chem. Phys.*, 1997, **106**, 4499–4508.

75 C. Lifshitz, *Eur. J. Mass Spectrom.*, 2002, **8**, 85–98.

76 R. A. Marcus, *J. Chem. Phys.*, 1952, **20**, 359–364.

77 H. J. C. Berendsen, D. van der Spoel and R. van Drunen, *Comput. Phys. Commun.*, 1995, **91**, 43–56.

78 E. Lindahl, B. Hess and D. van der Spoel, *Mol. Modeling Annual*, 2001, **7**, 306–317.

79 D. Van Der Spoel, E. Lindahl, B. Hess, G. Groenhof, A. E. Mark and H. J. C. Berendsen, *J. Comput. Chem.*, 2005, **26**, 1701–1718.

80 B. Hess, C. Kutzner, D. van der Spoel and E. Lindahl, *J. Chem. Theory Comput.*, 2008, **4**, 435–447.

81 S. Pronk, S. Páll, R. Schulz, P. Larsson, P. Bjelkmar, R. Apostolov, M. R. Shirts, J. C. Smith, P. M. Kasson, D. van der Spoel, B. Hess and E. Lindahl, *Bioinformatics*, 2013, **29**, 845–854.

82 M. J. Abraham, T. Murtola, R. Schulz, S. Páll, J. C. Smith, B. Hess and E. Lindahl, *SoftwareX*, 2015, **1–2**, 19–25.

83 S. Páll, A. Zhmurov, P. Bauer, M. Abraham, M. Lundborg, A. Gray, B. Hess and E. Lindahl, *J. Chem. Phys.*, 2020, **153**, 134110.

84 T. Lu, *Sobtop, Beijing Kein Research Center for Natural Sciences*, Beijing, 2023, vol. 1.0.

85 M. J. Frisch, G. W. Trucks, H. B. Schlegel, G. E. Scuseria, M. A. Robb, J. R. Cheeseman, G. Scalmani, V. Barone, G. A. Petersson, H. Nakatsuji, X. Li, M. Caricato, A. V. Marenich, J. Bloino, B. G. Janesko, R. Gomperts, B. Mennucci, H. P. Hratchian, J. V. Ortiz, A. F. Izmaylov, J. L. Sonnenberg, D. Williams-Young, F. Ding, F. Lipparini, F. Egidi, J. Goings, B. Peng, A. Petrone, T. Henderson, D. Ranasinghe, V. G. Zakrzewski, J. Gao, N. Rega, G. Zheng, W. Liang, M. Hada, M. Ehara, K. Toyota, R. Fukuda, J. Hasegawa, M. Ishida, T. Nakajima, Y. Honda, O. Kitao, H. Nakai, T. Vreven, K. Throssell, J. A. Montgomery Jr., J. E. Peralta, F. Ogliaro, M. J. Bearpark, J. J. Heyd, E. N. Brothers, K. N. Kudin, V. N. Staroverov, T. A. Keith, R. Kobayashi, J. Normand, K. Raghavachari, A. P. Rendell, J. C. Burant, S. S. Iyengar, J. Tomasi, M. Cossi, J. M. Millam, M. Klene, C. Adamo, R. Cammi, J. W. Ochterski, R. L. Martin, K. Morokuma, O. Farkas, J. B. Foresman and D. J. Fox, *Gaussian 16 Rev. B.01*, Gaussian, Inc., Wallingford, CT, 2016.

86 O. Ghasemalizadeh, S. Khaleghian and S. Taheri, *Int. J. Adv. Res.*, 2016, **4**, 1668–1686.

87 W. Humphrey, A. Dalke and K. Schulten, *J. Mol. Graphics*, 1996, **14**, 33–38.

88 K. K. Baldridge, M. S. Gordon, R. Steckler and D. G. Truhlar, *J. Phys. Chem.*, 1989, **93**, 5107–5119.

89 W. L. Hase, *Advances in Classical Trajectory Methods, Intramolecular and Nonlinear Dynamics*, JAI, Greenwich, Conn., 1992, vol. 1.

90 K. Bolton, W. L. Hase and G. H. Peslherbe, in *Modern Methods for Multidimensional Dynamics Computations in Chemistry*, ed. D. L. Thompson, World Scientific, Singapore, 1998, pp. 143–189.

91 V. Bakken, J. M. Millam and H. B. Schlegel, *J. Chem. Phys.*, 1999, **111**, 8773–8777.

92 X. Hu, W. L. Hase and T. Pirraglia, *J. Comput. Chem.*, 1991, **12**, 1014–1024.

93 W. L. Hase, K. Bolton, P. de Sainte Claire, R. J. Duchovic, X. Hu, A. Komornicki, G. Li, K. Lim, D. Lu, G. H. Peslherbe, K. Song, K. N. Swamy, S. R. Vande Linde, A. Varandas, H. Wang and R. J. Wolf, *VENUS 99: A General Chemical Dynamics Computer Program*, Texas Tech University Lubbock, TX, 1999.

94 G. H. Peslherbe, H. Wang and W. L. Hase, *Adv. Chem. Phys.*, 1999, **105**, 171–201.

95 J. Liu, W. Zhou, S. D. Chambreau and G. L. Vaghjiani, *J. Phys. Chem. B*, 2019, **123**, 2956–2970.

96 J. Liu, W. Zhou, S. D. Chambreau and G. L. Vaghjiani, *J. Phys. Chem. B*, 2020, **124**, 4303–4325.

97 W. Zhou, J. Liu, S. D. Chambreau and G. L. Vaghjiani, *J. Phys. Chem. B*, 2020, **124**, 11175–11188.

98 I. M. Alecu, J. Zheng, Y. Zhao and D. G. Truhlar, *J. Chem. Theory Comput.*, 2010, **6**, 2872–2887.

99 G. Wang and R. B. Cole, in *Electrospray Ionization Mass Spectrometry: Fundamentals, Instrumentation, and Applications*, ed. R. B. Cole, John Wiley & Sons, Inc, New York, 1997, pp. 137–174.

100 S. Castro, C. Larriba, J. F. D. L. Mora, P. Lozano and S. Sümer, 42nd AIAA/ASME/SAE/ASEE Joint Propulsion Conference & Exhibit, Sacramento, CA, 2012.

101 K. M. Ervin and P. B. Armentrout, *J. Chem. Phys.*, 1985, **83**, 166–189.

102 P. B. Armentrout, K. M. Ervin and M. T. Rodgers, *J. Phys. Chem. A*, 2008, **112**, 10071–10085.

103 W. D. Luedtke, U. Landman, Y. H. Chiu, D. J. Levandier, R. A. Dressler, S. Sok and M. S. Gordon, *J. Phys. Chem. A*, 2008, **112**, 9628–9649.

